UNIVERSITY *of* York

This is a repository copy of *Coded apertures with scatter and partial attenuation for high-energy high-resolution imaging*.

White Rose Research Online URL for this paper:
https://eprints.whiterose.ac.uk/id/eprint/163434/

Version: Published Version

White Rose
university consortium
Universities of Leeds, Sheffield & York

eprints@whiterose.ac.uk
https://eprints.whiterose.ac.uk/

PAPER • OPEN ACCESS

Coded apertures with scatter and partial attenuation for high-energy high-resolution imaging

View the article online for updates and enhancements.

Coded apertures with scatter and partial attenuation for high-energy high-resolution imaging

M P Selwood[1] , **C I D Underwood**[1] , **R Heathcote**[2] **and C D Murphy**[1]

[1] York Plasma Institute, Department of Physics, University of York, York, YO10 5DQ
[2] Central Laser Facility, Science and Technology Facilities Council, Rutherford Appleton Laboratory, Oxfordshire, OX11 0QX

E-mail: matthew.selwood@york.ac.uk

CrossMark

Abstract

Laser-plasma x-ray sources have garnered interest from various communities due to their ability to generate high photon-energies from a small source size. The passive imaging of high energy x-rays and neutrons is also a useful diagnostic in laser-driven fusion capsules as well as laboratory astrophysics experiments which aim to study small samples of transient electron-positron plasmas.

Here we study a coded aperture with scatter and partial attenuation included, which we call a 'CASPA', and compare them to the more common method of pinhole imaging. As well as discussing the well-known increased throughput of coded apertures, we also show that the decoding algorithm relaxes the need for a thick substrate. We simulate a 511 keV x-ray source through ray-tracing and Geant4 simulations to show how incomplete attenuation of the source by the mask may be less detrimental to imaging using a CASPA than to using a standard pinhole system.

Keywords: coded aperture, CASPA, x-ray imaging, neutron imaging, high-resolution, laser-plasma sources

(Some figures may appear in colour only in the online journal)

1. Introduction

Sub-millimetre radiation sources are ubiquitous in laser-plasma physics, from the small x-ray sources produced for imaging [1], to understanding fusion targets [2–4] or astrophysical analogues [5] including those which aim to study pure electron-positron plasmas [6]. Some such sources will also produce other forms of high-energy radiation—for instance the 14.1 MeV neutrons from DT fusion reactions. In addition, laser-based sources have the potential to impact medical or industrial imaging by increasing the photon energy accessible while potentially reducing the source size. This research into novel sources increases the urgency to find a method for imaging highly penetrating (> 100 keV), small (~ 10 μm) sources to aid development and optimisation.

Laser wakefield acceleration (LWFA) has demonstrated the ability to produce micron-sized, MeV-to-GeV electron beams over millimetre scales [7–10]. In addition, laser-plasma interactions have recently demonstrated the ability to produce intense beams of positrons [6, 11, 12]. In order to optimise x-ray sources from LWFA, or measure the spatial extent and charge of a positron population, improvements in the imaging of ~ 511 keV radiation sources would be advantageous.

2. Aperture imaging

Simple to implement, pinhole cameras provide one such solution, but are limited when in low signal or high energy

applications, due to the small pinhole size and attenuation requirement respectively. Since the resolution of the imaging system is dependent on the size of the pinhole, there is an inherent trade-off between imaging resolution and signal strength. In order to optimise a novel laser-based x-ray source (which may fluctuate from shot-to-shot), high resolution in a single shot is desirable. In addition, since the pinhole comprises only a small fraction of the substrate plane, the material used to form the pinhole must provide almost complete attenuation, requiring a thick substrate. Current micro-machining methods are limited to a hole aspect ratio of *ca.*50 [13] so again the resolution must be compromised for signal to noise ratio (SNR).

In response to these limitations, multi-pinhole systems have been employed, either in the form of a pinhole array [14, 15], or a coded aperture [16]. Both are multiple pinhole systems with differing methodologies; the former generates multiple images which can be added to compensate for low signal levels or can provide spectral information through differential filtering [17], whereas the latter superimposes the image from each pinhole, which is then decoded in a post-processing step. The specifics of coded apertures are discussed more in section 3, but they have have been implemented in a variety of ways, including time modulated apertures [18], spherical apertures for 3D reconstruction [19] and for imaging scattered x-rays in a medical context [20].

Both pinhole arrays and conventional coded apertures still require that the pinhole substrate be highly attenuating to achieve an acceptable SNR. Coded apertures are typically favoured for low-signal environments due to the larger number of perforations possible whilst using standard detectors. However, this is at the detriment of increased noise introduced from the decoding process, which is not present in pinhole array systems.

Where a static, passive aperture is used, coded apertures have been demonstrated to work for 0.06–1.3 MeV x-rays, requiring aperture perforation diameters of 1.3–2.2 mm [21]. Here, we demonstrate that the resolution limit may be extended by orders of magnitude, since the decoding process is able to discard the background arising from imperfect attenuation. This is quantified through ray tracing calculations which consider the aperture to be either scattering or only partially attenuating, allowing the impact of each effect on imaging capability to be studied independently. We then illustrate the effectiveness of a more realistic aperture—which will exhibit both effects—through Geant4 simulations of a point source. The theoretical imaging improvement expected using a Coded Aperture with Scattering and Partial Attenuation (CASPA) is compared to a pinhole of equivalent resolution and substrate thickness.

3. Coded apertures & CASPAs

A coded aperture is an array of κ pinholes—or *perforations*—in a specific arrangement, with each casting an image of the object onto the detector. The resultant signal from the overlaid images is dubbed the *hologram* [22]. This hologram can then

be decoded through a cross correlation against the decoding function (created from the known aperture design) to form a likeness of the original object [23–25].

In contrast to single pinholes, coded apertures do not have any inherent compromise between resolution and signal intensity. The signal may be increased by having a larger number of small perforations, since the resolution is still dictated by the perforation size, where as the signal strength is improved by a factor of κ. Usefully, another advantage of coded apertures is that the decoding process is uniform-background subtracting. The decoding functions are designed such that their cross correlation with an array of uniform magnitude is zero [26]. Thus, particles incident on the coded aperture need not be fully attenuated, as conventionally assumed, but merely scattered uniformly across the detector surface.

CASPAs utilize this property to propose apertures with better resolution than previously attainable when imaging high-energy x-rays (> 100 keV). When the combination of the scattered and non-scattered photons from the mask (pink and green in figure 1, respectively) creates a quasi-uniform background, and their intensity is lower than that of the signal (white), the object can still be reconstructed without the need for full attenuation. This increases the potential scope of use for CASPAs beyond that of pinhole arrays, as the latter does not contain a decoding method and thus is unable to compensate for partially attenuating substrates in a manner similar to the single pinhole case discussed in section 6.

Many coded aperture designs exist [27], each sharing similar principals: reduction of inherent noise achieved through uniform perforation distribution without translational symmetry, and maximization of the number of pinholes on the design [24]. For the purposes of this study, the Modified Uniformly Redundant Array (MURA) of Gottesman and Fenimore [25] is chosen as the CASPA. These are a family of coded apertures, where each design is designated by its individual prime number basis, *p*.

4. Ray-tracing model

A ray tracing model (RTM) has been used to generate synthetic holograms as follows: A ray, represented by unit-vector $\vec{r}$, is generated in a random direction from the source to the aperture. The distance between the between source and aperture in the direction of $\vec{r}$ is given by τ:

$$\tau = \frac{(\vec{P_a} - \vec{P_s}) \cdot \vec{n}}{\vec{r} \cdot \vec{n}} \tag{1}$$

where $\vec{P_a}$ is the position of the centre of the aperture, $\vec{P_s}$ is the position of the source, and $\vec{n}$ is the vector normal to the plane of the aperture. The impact point of $\vec{r}$ on the aperture, $\vec{P_i}$ is:

$$\vec{P_i} = \vec{P_s} + \tau \vec{r} \tag{2}$$

If $\vec{P_i}$ is within the given aperture dimensions, it is compared against the aperture to test if the impact is at a perforation site, of size A_{pix}. Then, the rays are:
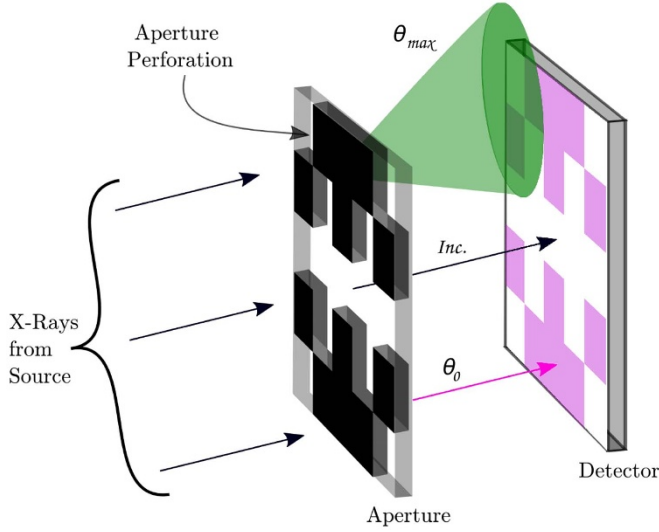
Figure 1. CASPA system, using a $p = 5$ MURA. X-rays pass through perforations (black), or strike the substrate and are unscattered (pink) or scattered (green).

(a) absorbed and removed from the simulation;
(b) scattered by angle θ;
(c) incident on a perforation and unaffected.

The likelihood of absorption and the maximum scattering angle, $\theta_{\max}$, may be varied in the simulation. The scattering vector $\delta\vec{r}$ is given by:

$$z = R(1 - \cos\theta) + \cos\theta \tag{3}$$

$$y = \sin\phi\sqrt{1 - z^2} \tag{4}$$

$$x = \cos\phi\sqrt{1 - z^2} \tag{5}$$

where R, ϕ and θ are uniformly distributed random numbers within the ranges: $0 \leq R \leq 1$, $0 \leq \phi < 2\pi$ and $0 \leq \theta \leq \theta_{\max}$. This is added in summation to $\vec{r}$ and normalised, to create a perturbed unit vector. Equations (1) and (2) are re-applied to all the scatter and perforation site rays, using the position of the detector, $\vec{P_d}$ instead of $\vec{P_a}$, to find the new $\vec{P_i}$ in the detector plane. A hologram is then constructed from a histogram of the detector plane.

Once decoded, the image is evaluated by calculating the SNR from the known position of the sources in the object plane:

$$\mathrm{SNR}_j = \frac{\lambda_j - \mu_{\bar{j}}}{\sigma_{\bar{j}}} \tag{6}$$

where j is the set of expected positions, λ_j is the sum of signal strength over all j and $\mu_{\bar{j}}$ and $\sigma_{\bar{j}}$ are the mean and standard deviation of all pixels not in set j, respectively. All pixels not in set j are henceforth called the background.
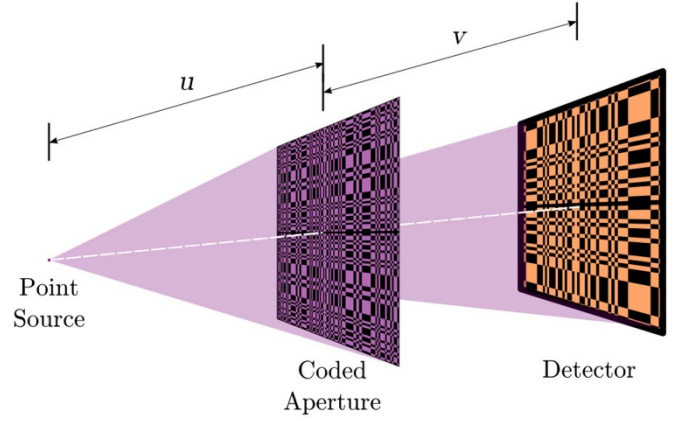

Figure 2. A diagram of the CASPA imaging system used in this study, using a RTM generated hologram on the detector. The aperture is a $p = 53$ MURA, and $u = v = 1060A_{\mathrm{pix}}$.

5. Experimental considerations

In this design study, a $p = 53$ MURA is used, which has 5512 perforations. 6×10^7 photons are randomly fired at the aperture from the point source and collected on a detector of idealised dimensions, as depicted in figure 2. The system has a magnification of 1 [26, 28], and no addition of external noise or background. The idealised detector size, D_{det} is given by:

$$D_{\mathrm{det}} = \frac{Mp}{R} \tag{7}$$

where M is the magnification of the system and R is the desired number of resolvable features per unit length, henceforth called resolution capability. The pixel size of the idealised detector is given by:

$$D_{\mathrm{pix}} = \frac{M}{nR} \tag{8}$$

where n is any positive integer, and the aperture pixel size is given by:

$$A_{\mathrm{pix}} = \frac{1}{R(M^{-1} + 1)} \tag{9}$$

For this study the detector is 106×106 pixels, $R = 0.5$ pixel^{-1}, $M = 1$ and $n = 2$, resulting in aperture and detector pixels being the same size. The imaging system field-of-view will be proportional to the size of the aperture p value and the desired resolution capability. As such, for any other given experiment a detector can be chosen to fit the spatial and spectral requirements.

While this work does not aim to resolve the challenges in selecting an appropriate detector, it is clear that MeV-photon or neutron detection with sub-100 μm resolution is not possible with high efficiency. Mikerov *et al* [29] suggest that neutron detector resolution could be better than 100 μm. With modest magnification built in to system, the increased throughput of a CASPA could be beneficial for imaging the symmetry of DT-fusion reactions in inertial confinement
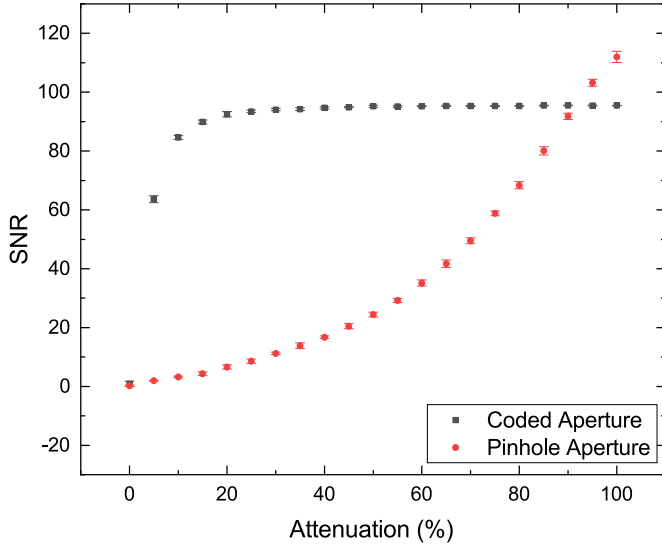
Figure 3. Variation in SNR for coded and pinhole apertures as a function of aperture attenuation only. Errors from the standard deviation of 6 simulations.
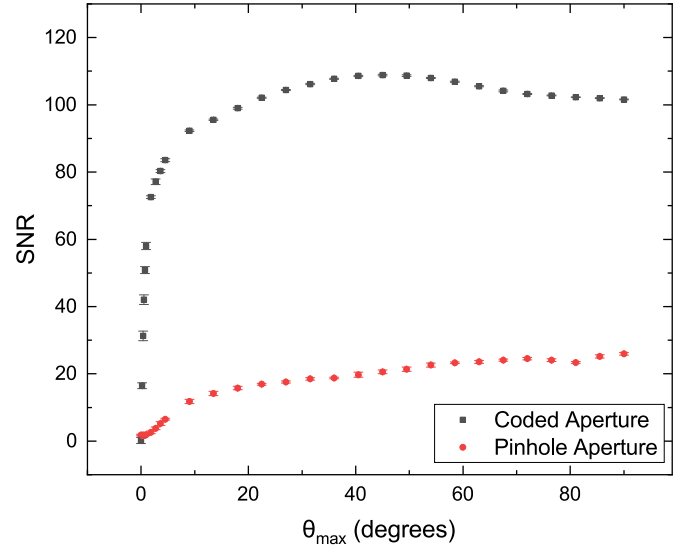

Figure 4. Variation in SNR for coded and pinhole apertures as a function of θ_{max}. Zero attenuation is assumed. Errors from the standard deviation of 6 simulations.

fusion experiments. For a resolution of 0.1 μm^{-1} as indicated in this work we would require a detection area in excess of 0.5 × 0.5 mm, and a pixel size of ≤10 μm. At photon energies < 30 keV, this can be readily achieved with commercially available sCMOS detectors, whilst the 30–100 keV range can be achieved with CdTe detectors [30]. Detectors in the 200+ keV range are under development, such as a CsI array [31], and the progress of other such high-energy, high-resolution detectors will be concurrent with development in compact laser-plasma x-ray sources and fusion neutron detectors. CASPAs are not reliant on such development, and can be used with current detectors and system magnification to achieve the desired resolution capability.

6. CASPA—pinhole comparison

We now compare a CASPA to a standard pinhole, as a function of the substrate properties using SNR as defined above as the figure of merit. Although SNR will be a function of the number of particles used (either photon or neutron), and thus SNR values are not absolute, their relative values and trends are of use. For the initial comparison, it is assumed that aperture attenuation and maximum scattering angle can be varied independently. While these properties will be correlated and dependent on the physical attributes of the aperture, it is useful to consider their effects on image quality independently.

The detrimental effect of incomplete attenuation on a pinhole aperture can be seen in figure 3. It follows the expected trend, due to the lack of inherent background-subtraction. In contrast, the SNR of the coded aperture remains within 5% of its maximum at only 15% attenuation. It should be noted that, since the decoding is conducted in Fourier space with finite planes, the coded aperture always exhibits noise even at 100% attenuation and so underperforms the pinhole in this case.
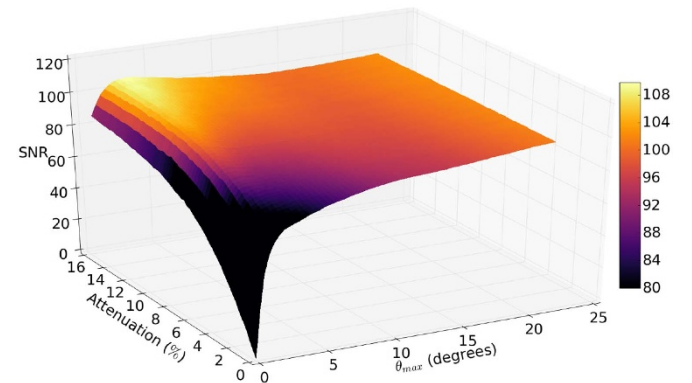

Figure 5. Surface plot of SNR as a function of both attenuation and θ_{max}.

From figure 4, it is clear that scattering through the aperture is of limited value to imaging with a pinhole. The increase in SNR here is, in small part, due to scattered particles missing the detector. The more significant effect is that the scattered rays are being distributed over a larger area. In the case of the coded aperture, this quasi-uniform background will be removed during decoding, resulting in a near-zero $\mu_{\bar{j}}$. However, in the case of the pinhole the quasi-uniform background remains, increasing $\mu_{\bar{j}}$ and thus reducing the SNR of the pinhole. This effect has reduced the SNR maximum of the pinhole by 83%, compared with the maximum seen in figure 3.

Individually, figures 3 and 4 show that SNR of a CASPA is not degraded when the substrate has a minimum attenuation of 15% or a minimum θ_{max} of 8°. The two mechanisms can be combined to produce a CASPA with lower values of each, whilst still keeping sufficient SNR to allow imaging. The results of a two dimensional study (figure 5) demonstrate this additive effect.

7. Benchmarking RTM with geant4

Although the RTM is useful in demonstrating the independent effects of scattering and attenuation on imaging efficacy, it does not reflect the reality that both will increase as the aperture thickness is increased. For this, a Monte Carlo simulation package is required. 511 keV photons are used, to coincide with gamma rays used in PET imaging [32] and the CASPA and source are modelled using Geant4 [33].

To benchmark the RTM, the same design and geometry is modelled in Geant4. A 250 μm thick tungsten substrate was used, equivalent to 6.30% attenuation, with an A_{pix} of 50 μm, and thus an aspect ratio of 5.

It was found that, above an aspect ratio of 5-10, the effective field of view for many of the non-central CASPA perforations did not include the point source being imaged. This in an inherent issue with using MURAs, as they were originally designed for far-field imaging, instead of the near-field application being demonstrated here. To generate a 4π scattering source, a positron beam of 2^{32-1} particles was directed onto a 200 μm tungsten target, resulting in 1.34×10^6 photon events on the detector.

A separate Geant4 simulation was used to determine θ_{max}, in order to create a comparable environment for the RTM. 1×10^8 511 keV photons were fired into a 250 μm tungsten plate, and the FWHM of their impact upon the detector calculated. This resulted in a θ_{max} of 1.3 ± 0.2 degrees. It was also quantified that only 0.8% of the non-attenuated ray were scattered by the substrate, which was then incorporated into the RTM. 5.33×10^6 photons were used, in resulting in a comparable $(1.33 \pm 0.01) \times 10^6$ detector events.

The decoded images of the RTM and Geant4 can be seen in figure 6, with SNR values of 47 ± 3 and 43, respectively. The variation is likely due to the discrepancy in source size; the RTM source is an infinitesimally small point in space, whilst Geant4 source size is $1/4A_{pix}$, due to the intrinsic requirement for finite dimensions. The reduced SNR is due to the diminished number of photons impacting the detector with respect to section 6. However, the added complexity of the Geant4 toolkit makes higher Geant4 fluxes impractical due to the simulation run-time.

Despite the slight variation in SNR, figure 6 is able to show that the two hologram generation techniques are comparable. The RTM run-time is orders of magnitude smaller than its Geant4 counterpart, being 10's of seconds versus 10's of hours, and as such the RTM is preferred for simulating higher flux systems.

8. Extended object

Generating a hologram for an extended object requires an increase in number of particles used, to prevent a significant drop in intensity per unit area in the source plane, or *object plane* now an extended shape is being imaged. As RTM holograms were shown to be comparable to Geant4, RTM is used for the extended object, due to its greater speed.
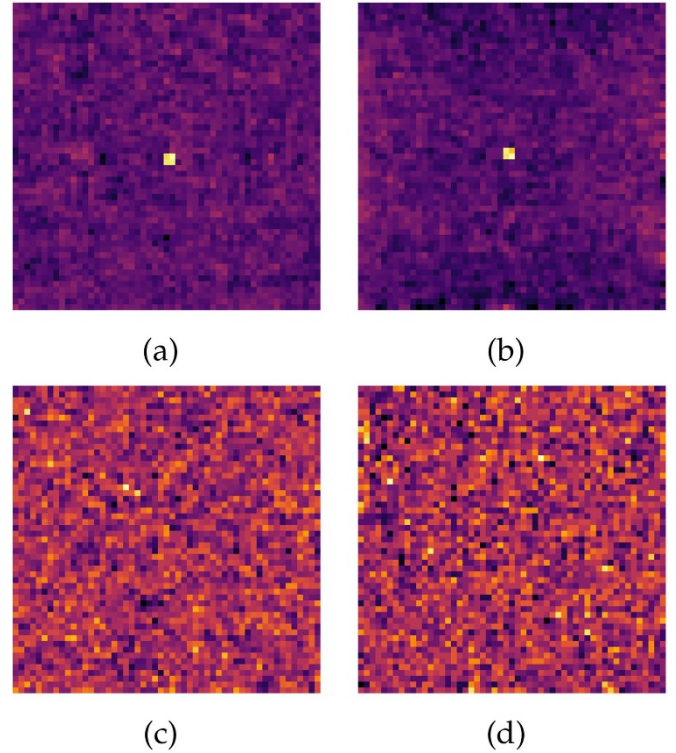

(a)

(b)

(c)

(d)

Figure 6. A comparison between the RTM, (a) & (c), and Geant4, (b) & (d), methods for holgram simulation. (a) & (b) use a CASPA, whilst (c) & (d) are pinholes. (a)–(d) all have the same substrate thickness and A_{pix}. The scales are independent of one another, ranging from the local minima to maxima, with the CASPAs being the expected *circa* 2 orders of magnitude greater than the pinholes.

Continuing with the example of a tungsten aperture to image 511 keV photons, a substrate thickness of 18 mm would be required for 99% attenuation. This would impose a theoretical resolution limit of 7 mm at an aspect ratio of 5, although in practice the thickness is likely to render the camera unsuitable for this energy. This is in contrast to the 250 μm CASPA, with a theoretical resolution limit of 100 μm. This equates to a $\times 70$ increase in resolution capability in this demonstration. Moreover, the CASPA (figure 7(a)) is able to reconstruct an image in the high-energy low-signal environment that an equivalent pinhole (figure 7(b)) could not.

We propose that extending the aperture-detector distance could further decrease the aperture thickness required for effective imaging. Scatter within a CASPA enables a high SNR by distributing the photons upon a large detector area, creating a quasi-uniform background. By conserving the detector area over which photons are scattered, it can be shown geometrically that θ_{max} and the aperture-detector distance are inversely proportional. As propagation distance has not been investigated here, its effects can instead be qualitatively discussed through an increase in θ_{max}. An increase in θ_{max} has been shown by figure 5 to require less aperture attenuation, and therefore can produce a better imaging resolution; this is before considering the classical resolution improvement from system magnification.
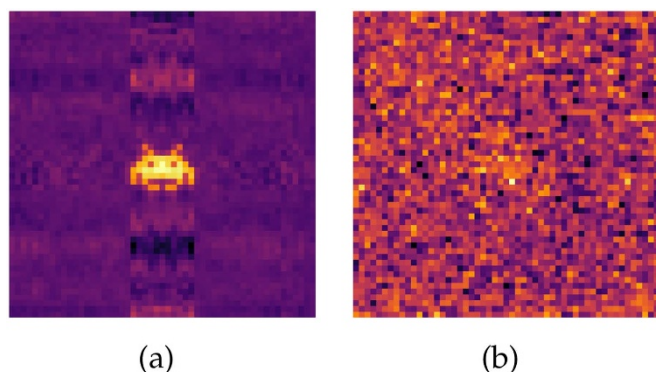
Figure 7. RTM generated results for a CASPA (a), and an equivalent pinhole (b) for an extended object. 1×10^8 photons per object unit area, resulting in a total flux of 4.6×10^9 511 keV photons.

9. Conclusion

In summary, we propose that complete attenuation is not required for coded apertures to generate high SNR images. We demonstrate that this benefit is due to the way in which the image from a coded aperture is reconstructed, allowing a flat background to be removed. This means that full-attenuation of the substrate is not required and that scattering the photons or neutrons through the aperture relaxes this requirement further. We also show through benchmarking with Geant4 that, with knowledge of the scattering angle and attenuation of the substrate, coded aperture holograms may be generated quickly from a ray tracing model.

We show a practical example of this by simulating an extended object imaged with 511 keV photons using a 250 μm thick tungsten CASPA. Through this, we demonstrate that high-energy low-flux aperture imaging is feasible, corresponding to a significant improvement in either resolution or flux compared to a fully attenuating pinhole aperture.

Acknowledgments

ORCID iDs

M P Selwood ⬤ https://orcid.org/0000-0002-9163-1857
C I D Underwood ⬤ https://orcid.org/0000-0002-1691-6377
C D Murphy ⬤ https://orcid.org/0000-0003-3849-3229

References

[1] Brenner C M *et al* 2015 Laser-driven x-ray and neutron source development for industrial applications of plasma accelerators *Plasma Phys. Control. Fusion* **58** 014039

[2] Bradley D K, Bell P M, Landen O L, Kilkenny J D and Oertel J 1995 Development and characterization of a pair of 30-40 ps x-ray framing cameras *Rev. Sci. Instrum.* **66** 716–18

[3] Oertel J A *et al* 2006 Gated x-ray detector for the national ignition facility *Rev. Sci. Instrum.* **77** 10E308

[4] Talebitaher A, Springham S V, Shutler P M E, Lee P and Rawat R S 2012 Imaging of plasma focus fusion by proton coded aperture technique *J. Fusion Energy* **31** 234–41

[5] Lebedev S V *et al* 2005 Magnetic tower outflows from a radial wire array Z-pinch *Mon. Not. R. Astron. Soc.* **361** 97–108

[6] Sarri G *et al* 2015 Generation of neutral and high-density electron–positron pair plasmas in the laboratory *Nat. Commun.* **6** 6747

[7] Tajima T and Dawson J M 1979 Laser electron accelerator *Phys. Rev. Lett.* **43** 267–70

[8] Mangles S P D *et al* 2004 Monoenergetic beams of relativistic electrons from intense laser-plasma interactions *Nature* **431** 535–8

[9] Geddes C G R, Toth C, Van Tilborg J, Esarey E, Schroeder C B, Bruhwiler D, Nieter C, Cary J and Leemans W P 2004 High-quality electron beams from a laser wakefield accelarator using plasma-channel guiding *Nature* **431** 538–41

[10] Faure J, Glinec Y, Pukhov A, Klselev S, Gordienko S, Lefebvre E, Rousseau J P, Burgy F and Malka V 2004 A laser-plasma accelerator producing monoenergetic electron beams *Nature* **431** 541–4

[11] Chen H *et al* 2010 Relativistic quasimonoenergetic positron jets from intense laser-solid interactions *Phys. Rev. Lett.* **105** 015003

[12] Sarri G *et al* 2013 Table-top laser-based source of femtosecond, collimated, ultrarelativistic positron beams *Phys. Rev. Lett.* **110** 255002

[13] Hof L A and Ziki J A 2017 Micro-hole drilling on glass substrates-A review *Micromachines* **8** 53

[14] Yaakobi B, Marshall F J and Bradley D K 1998 Pinhole-array x-ray spectrometer for laser-fusion experiments *Appl. Opt.* **37** 8074–80

[15] Labate L *et al* 2007 Novel x-ray multispectral imaging of ultraintense laser plasmas by a single-photon charge coupled device based pinhole camera *Rev. Sci. Instrum.* **78** 103506

[16] Greenberg J A, Lakshmanan M N, Brady D J and Kapadia A J 2015 Optimization of a coded aperture coherent scatter spectral imaging system for medical imaging *Medical Imaging 2015: Physics of Medical Imaging* ed Hoeschen C, Kontos D and Flohr T G Bellingham, Washington USA Int. Society for Optics and Photonics vol 9412 p 94125E

[17] Wagner R F, Brown D G and Metz C E 1981 On The Multiplex Advantage Of Coded Source/Aperture Photon Imaging *Digital Radiography* editor Brody W R Bellingham, Washington USA Int. Society for Optics and Photonics vol 0314 pp 72–6

[18] Wang D, Ruskov I N, Hu H, Kopatch Y N, Grozdanov D N, Fedorov N A and Aliyev F A 2019 Gamma-ray imaging with a time-modulated random coded aperture *Rev. Sci. Instrum.* **90** 015107

[19] Hellfeld D, Barton P, Gunter D, Mihailescu L and Vetter K 2017 A spherical active coded aperture for 4π gamma-ray imaging *IEEE Trans. Nucl. Sci.* 1–1

[20] Krishnamurthy K, Sahbaee P, Chawla A, Wolter S, Maccabe K, Brady D, Samei E, Kapadia A J and Lakshmanan M N 2013 Monte-carlo simulations of a coded-aperture x-ray scatter imaging system for molecular imaging *Medical Imaging 2013: Physics of Medical Imaging* SPIE Medical Imaging vol 8668

[21] Ivanov O P, Sudarkin A N, Stepanov V E and Urutskoev L I 1999 Portable X-ray and gamma-ray imager with coded mask: performance characteristics and methods of image

reconstruction *Nucl. Instruments Methods Phys. Res. Sect.* A **422** 729–34

[22] Mertz L and Young N O 1961 Fenzel Transform Images *Int. Conf. Opt. Instruments Tech.* (London: Chapman and Hall) pp 305–10

[23] Papoulis A 1962 *The Fourier Integral and its Applications* (New York: McGraw-Hill)

[24] Fenimore E E and Cannon T M 1978 Coded aperture imaging with uniformly redundant arrays *Appl. Opt.* **17** 337

[25] Gottesman S R and Fenimore E E 1989 New family of binary arrays for coded aperture imaging *Appl. Opt.* **28** 4344

[26] Selwood M P, Heathcote R and Murphy C D 2018 Imaging objects with coded apertures, utilising a laser wakefield x-ray source *16th Int. Conf. X-Ray Lasers* Springer Proc. in Physics Series

[27] Cieślak M J, Gamage K A A and Glover R 2016 Coded-aperture imaging systems: Past, present and future development – A review *Radiat. Meas.* **92** 59–71

[28] Heathcote R, Booth N, Clarke R J, Anderson-Asubonteng A, Selwood M P and Spindloe C 2018 Coded aperture x-ray imaging of high power laser-plasma interactions on the Vulcan Laser System ed Grim G P, Bradford Barber H, Furenlid L R and Koch J A *Radiat. Detect. Med. Ind. Natl. Secur. XIX* SPIE vol 10763 p 29

[29] Mikerov V I *et al* 2004 Prospects for efficient detectors for fast neutron imaging *Applied Radiation and Isotopes* **61** 529–35 Proc. of the Fourth Int. Topical Meeting on Neutron Radiography. Advances in Neutron Imaging for the 21st Century

[30] Seller P, Veale M C, Sellin P J, Jacques S D M, Cernik R J, Scuffham J W and Wilson M D 2012 A CdTe detector for hyperspectral SPECT imaging *J. Instrum.* **7** P08027–P08027

[31] Armstrong C *et al* 2016 Pulsed x-ray imaging of high-density objects using a ten picosecond high-intensity laser driver *Emerging Imaging Sensing Technol.* **9992**

[32] Moses W W 2011 Fundamental Limits of Spatial Resolution in PET. *Nucl. Instrum. Methods Phys. Res.* A **648** Supplement 1 S236–S240

[33] Agostinelli S *et al* 2003 GEANT4—A simulation toolkit *Nucl. Instruments Methods Phys. Res. Sect.* A **506** 250–303